This article has been accepted for publication in a future issue of this journal, but has not been fully edited. Content may change prior to final publication. Citation information: DOI 10.1109/ACCESS.2021.3108462, IEEE Access

Feature extraction of laser welding pool image and application in welding quality identification

YINRUI GAO[1], PING ZHONG[1], XIN TANG[2], HAOWEI HU[1] and PENG XU[1]

[1]College of Science, Donghua University, Shanghai 201620, China
[2]College of Information Science and Technology, Donghua University, Shanghai 201620, China

Corresponding author: Ping Zhong (pzhong937@dhu.edu.cn).

This work was supported by the National Natural Science Foundation of China under Grant 51975116 and in part supported by the Natural Science Foundation of Shanghai under Grant 21ZR1402900.

ABSTRACT Most of the existing laser welding quality identification methods are post-weld identification or low-speed identification (Welding speed below 120m/min). Efficiently online monitoring of laser welding can take the advantages of laser welding for high-speed and deep-penetration welding. How to eliminate interference information (such as metal vapor, plasma splash, etc.) in the laser welding process, accurately and quickly extract the feature information of welding quality evaluation, and identify defects is a major problem that laser welding online monitoring technology needs to solve urgently. In this paper, the optimized dark channel prior anti-interference processing algorithm can remove the interference of image. The feature information extraction algorithm based on contour and OTSU threshold segmentation are used to extract the features of the welding image that collected by the image acquisition system. Then, the image is classified as a specific defect by the trained BP neural network classification algorithm. Experiments with 304 stainless steels have proved that this method can effectively remove the interference of metal vapor and plasma splash on the feature information, and achieves 97.18% accuracy rate of the binary classification test and 91.29% accuracy rate of the six-classification test. The processing time of the entire algorithm is about 0.3ms and it can meet the real-time requirements of high-speed laser welding.

INDEX TERMS Anti-interference processing, Online quality evaluation, Laser welding, Machine learning

I. INTRODUCTION

As a new type of welding technology, laser welding is one of the most ideal technologies to realize high-speed and deep-penetration welding. Because of its high energy density and ability to weld heterogeneous materials [1], it is developing rapidly in the field of industrial processing and modern intelligent manufacturing [2-4]. However, due to various process parameters, defects inevitably occur in laser welding.

The current non-destructive testing methods for the quality of laser welding welds are mainly post-weld testing and low-speed online monitoring. It is mainly divided into welding internal defect detection methods (such as: radiation [5-9], ultrasonic [10-14], etc.), welding surface defect detection methods (such as: visual [15, 16], structured light [17-21], etc.) and on-line monitoring methods during low-speed welding (such as: short shutdown [22], near-infrared camera [23]). Post-weld identification also has disadvantages such as long identification times, low efficiency and poor traceability. In some cases, complete identification is not possible and only sampling identification can be performed.

Miao *et al.* proposed a weld quality recognition method based on CNN (Convolutional Neural Network) that has the advantage of high accuracy [24], and the time for single identification is 3.2s, but this 3.2s processing time is too long for synchronous detection. Indimath *et al.* proposed a welding defect detection method based on ultrasonic that requires a short shutdown of the production equipment for detection [22]. Dorsch *et al.* proposed a weld feature detection method based on the near-infrared camera [23] that is difficult to achieve ultra-high frame rate detection and complete identification in high-speed laser welding (120m/min and above).

In order to solve the many shortcomings of the above-mentioned detection methods, it is of great significance to develop online monitoring technology of laser welding quality that can simultaneously monitor the quality of weld during the welding process. Therefore, monitoring the welding process through machine vision and image processing technology, and simultaneously extracting important information for evaluating welding quality during the welding process, is the hot direction for solving the above-mentioned problems.

This article has been accepted for publication in a future issue of this journal, but has not been fully edited. Content may change prior to final publication. Citation information: DOI 10.1109/ACCESS.2021.3108462, IEEE Access

However, when images are acquired continuously, the keyhole boundaries are heavily disturbed by bright light. Therefore, many scholars in the world have studied various imaging methods and image processing methods [4, 25-30]. Katayama *et al.* studied the reflected laser beam and radiated light as monitoring signals during laser welding of aluminum alloys to elucidate the correlation between monitoring signals and welding phenomena during the formation of weld defects [30]. Wen and Gao used a high-speed camera to acquire images of the plume generated during laser welding in the UV and visible wavelengths, and then classified the samples by using the feature parameters of the splash images and the k-nearest neighbor classification method. As the result, the recognition rate is higher with the average gray level and entropy of the image as the feature parameters [31]. Zhang *et al.* used 660 nm and 850 nm filters to combine the images collected by the dual cameras to obtain a clear image of the weld pool and predict the width of the weld [32]. Chen *et al.* used a coaxial CCD camera installed on the welding head to shoot the molten pool, and studied the relationship between the area of the molten pool and the laser power, defocus distance, welding speed and other process parameters through various image processing algorithms [33].

Meanwhile, many different defect detection methods based on texture analysis have been proposed [34]. Fekri-Ershad *et al.* proposed a surface texture defect detection method based on single dimensional local binary patterns [35]. It has high detection rate and low computational complexity. Timm *et al.* performed Weibull features in texture defect detection [36]. It can detect local deviations of texture images in an unsupervised manner with high accuracy, and be applied in real-time applications. Susan et al. achieved an automated high accuracy texture defect detection method [37]. This method used non-extensive entropy with Gaussian gain as the regularity index and computed locally from texture patches through a sliding window approach. In the end, an automatic defect detection with no manual intervention was achieved.

On the other hand, machine learning algorithms such as neural networks are also widely used in the evaluation and classification of welding defects. Shevchik *et al.* [38] proposed an improved adaptive kernel algorithm. By using Gaussian mixture and complex features, the classification accuracy of this algorithm is between 85.9%-99.9%. Chen *et al.* obtained the plasma radiation information during welding by the optical fiber probe, classified the defects of optical fiber laser welding [39] by using the plasma spectral data and neural network algorithm, and compared the performance of SVM (Support Vector Machine) and neural network. Zhang *et al.* [40] built a multi-sensor laser welding monitoring system and used CNN (Convolutional Neural Networks) to classify three welding defects. The robustness of BP neural network was compared with that of CNN. Shevchik *et al.* [41] used hard X-ray radiography to obtain laser welding images. And a variety of CNN models are used to classify defects in X-ray images. The confidence of the defect classification ranges between 71% and 99%, and a computation time per classification task as low as 2 ms.

However, above approaches has their own shortcomings in different aspects. It has either too much time spending or too less accuracy. In addition, the device requirement of those approaches is much.

Due to the widespread use of laser welding in various industries, a more effective online quality identification method is needed to identify defects.

At present, ultrasonic, structural light and X-ray equipment are commonly used in laser welding quality inspection equipment, but the equipment is complex and the cost is high. In our study, only an ordinary camera is needed to monitor the welding quality, which greatly reduces the cost. However, camera imaging is easily disturbed by metal vapor and plasma splash, so feature information is lost seriously, and only contour information can be extracted. Using HU moment and BP neural network to identify defects can not only extract features well, but also meet the requirements of high-speed processing.

In this paper, the optimized dark channel prior anti-interference processing algorithm and the feature information extraction algorithm based on contour and OTSU threshold segmentation are used to extract the features of the welding image that collected by the image acquisition system. Then, the image is classified as a specific defect by the trained BP neural network classification algorithm. Experiments that using 304 stainless steels have proved that this method can effectively remove the interference of metal vapor and plasma splash on the feature information, and achieves 97.18% accuracy rate of the binary classification test and 91.29% accuracy rate of the six-classification test. The processing time of the entire algorithm is about 0.3ms and it can meet the real-time requirements of high-speed laser welding. In addition, the device has a simple structure and can monitor the quality of weld simultaneously during the welding process.

II. LASER WELDING QUALITY FEATURE EXTRACTION METHOD

During the laser welding process, the molten pool-keyhole movement contains a wealth of welding quality information, and the morphology feature of the molten pool-keyhole directly reflect the welding quality, weld morphology, welding defects and other conditions [42]. A high-speed camera can be used to obtain a clear image of the molten pool, and image processing technology is used to extract relevant feature information, such as the contour of the molten pool, the area of the molten pool, etc. Then statistical analysis methods are proper way to establish the relationship between the feature of the molten pool and welding defects [43]. In this way, the quality of laser welding can be judged.

In order to solve the existing problems, a method of morphology feature extraction for laser welding based on machine vision is proposed in this paper. This method uses anti-interference algorithms with different parameters for processing when extracting different features. And the

This article has been accepted for publication in a future issue of this journal, but has not been fully edited. Content may change prior to final publication. Citation information: DOI 10.1109/ACCESS.2021.3108462, IEEE Access

features can be extracted synchronously in the welding process and make full use of the fast laser welding speed.

In order to accurately extract the feature information of weld state, the following three steps are used in this method: (1) anti-interference pre-processing based on dark channel prior; (2) extraction of keyhole feature information based on contour characteristics; (3) extraction of weld feature information based on OTSU threshold segmentation. They are respectively used to exclude the interference information in the weld image, extract the keyhole feature information and the feature information of the weld width.

A. ANTI-INTERFERENCE PROCESSING BASED ON DARK CHANNEL PRIOR

According to a paper published by He in 2009, a haze removal algorithm based on dark channel prior was proposed [44], and the dark channel is defined as:

$$J^{\text{dark}}(\mathrm{x}) = \min_{c\in[R,G,B]}\left(\min_{\mathrm{y}\in\Omega(\mathbf{x})}\left(J^c(\mathrm{y})\right)\right), \tag{1}$$

where $J^{\text{dark}}(\mathrm{x})$ represents the dark channel value of the pixel $\mathbf{x}$; J^c represents each channel of the color image; $\Omega(\mathbf{x})$ represents a window centered on the pixel $\mathbf{x}$.

According to statistical experience, a haze-free image often has the conclusions as:

$$J^{\text{dark}} \to 0. \tag{2}$$

The prior statistical conditions in He's paper were obtained from 5,000 natural haze-free images. For the laser welding conditions described in this paper, the optimized dark channel prior algorithm is also effective for metal vapor and plasma splash, since the effects of metal vapor and plasma corona on the image are similar to those caused by haze in nature.

The atmospheric scattering model as:

$$I(x) = J(x)t(x) + A\big(1 - t(x)\big), \tag{3}$$

where $I(x)$ represents haze image; $J(x)$ represents haze-free image; A represents global atmospheric light intensity; $t(x)$ is the transmittance, that is, the part that is not scattered when the light enters the imaging device through the air.

The $I(x)$ means the light intensity which received by sensors. It is made up of two parts. One of it comes from object reflection. The $J(x)t(x)$ part of the equation represents that the light reflects from the object surface and it scatters before the sensor receives. Another one comes from light source. The $A\big(1 - t(x)\big)$ part of the equation represents that the light is emitted from the source and it also scatters before the sensor receives. The global atmospheric light intensity is hard to get from images, because it's light intensity when the light emitted from the source. In the algorithm, the atmospheric light intensity is estimated.

According to the atmospheric scattering model, only need to obtain the values of $t(x)$ and A to calculate the haze-free image $J(x)$. Since the welding image does not have a clear distinction between the front and back scenes, solving the global atmospheric light intensity A does not achieve good results when using the algorithm of OTSU thresholding of natural scenes and solving the global atmospheric light intensity in segments [45]. In our anti-interference algorithm, simply take the RGB pixel corresponding to one thousandth of the brightest pixel of the dark channel image, calculate the average value of the corresponding channel, and take this as the global atmospheric light intensity A, then good anti-interference effect can be obtained.

Global atmospheric light intensity formula as:

$$A^c = \frac{Sum^c}{N}, c \in [R, G, B], \tag{4}$$

where A^c represents atmospheric light intensity of the channel c; Sum^c represents sum of the values of channel c in the RGB pixels corresponding to the thousandth brightest pixel point of the dark channel image; N represents one thousandth of the total number of pixels in the original image.

Transmittance formula as:

$$t(x) = 1 - \omega \min_{c}\left(\min_{\mathrm{y}\in\Omega(x)}\left(\frac{I^c(y)}{A^c}\right)\right), \tag{5}$$

where I^c represents a haze image of channel c; ω represents retention coefficient of haze.

In the haze removal process of images with natural haze, the requirements for the solved transmittance $t(x)$ are relatively loose. Image areas with different depth of field also have certain light scattering in the absence of haze. For making the image more reality after haze removal, the retention coefficient ω of haze is usually 0.95. However, under laser welding conditions, there is almost no effect of depth of field, and the reflection of the metal plate around the weld is easily interpreted as part of the haze by the algorithm. If $\omega = 1$ is applied to the image, the edge of the weld is not clearly maintained. The test results are that when $\omega = 1$ (complete haze-free) extracting the keyhole feature information and when $\omega = 0.9$ (maintaining high contrast at the weld edge) extracting the weld feature information is a better option. To improve the computational speed, the gradient-oriented filtering method [46] is used in this paper to solve the transmittance.

In the process of solving the dark channel of natural scenery images, the commonly used $\Omega(\boldsymbol{x})$ range radius is 5-25 pixels. According to the characteristics of laser welding images, the smaller $\Omega(\boldsymbol{x})$ range can better remove the interference caused by metal vapor and plasma splash to the image. The edge of the feature will also be clearer.

B. KEYHOLE FEATURE INFORMATION EXTRACTION

When defects occur in the laser welding process, the morphology of the keyhole changes more obviously, and it is feasible to use the contour of the keyhole as the feature of welding defects. The contour of the keyhole in different welding states are shown in Fig. 1.

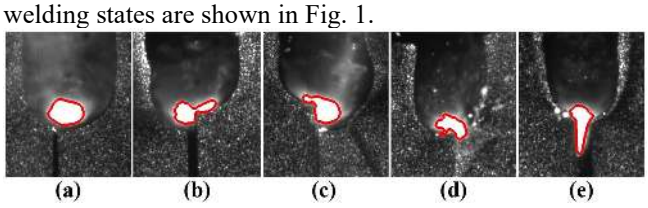

FIGURE 1. **(a)Sound well weld; (b), (c)Dislocation; (d)Inclusion; (e)Large gap.**

This article has been accepted for publication in a future issue of this journal, but has not been fully edited. Content may change prior to final publication. Citation information: DOI 10.1109/ACCESS.2021.3108462, IEEE Access

For a pure welding image, the contour of the keyhole can be extracted simply through the OpenCV API.

Since the contour image of the keyhole is relatively simple, the contour geometric moment [47] can be used to distinguish it, and it can meet the requirements of calculation speed and accuracy at the same time.

The n-order geometric moment of the contour as:

$$M_{i,j} = \sum_x \sum_y x^i y^j I(x,y), n = i + j \ (i,j = 0,1,2\cdots), \quad (6)$$

where $M_{i,j}$ represents the n-order geometric moment of the contour; $I(x,y)$ represents gray value at point (x,y).

The geometric central moment of the contour as:

$$\mu_{i,j} = \sum_x \sum_y (x-\bar{x})^i (y-\bar{y})^j I(x,y), \quad (7)$$

where $\mu_{i,j}$ represents the geometric central moment of the contour; $\bar{x}$, $\bar{y}$ represents the centroid of the contour, calculation formula as:

$$\bar{x} = \frac{M_{1,0}}{M_{0,0}}, \bar{y} = \frac{M_{0,1}}{M_{0,0}}. \quad (8)$$

The standardized central moment as:

$$\eta_{i,j} = \frac{\mu_{i,j}}{\mu_{00}^{\gamma}}, \gamma = \frac{i+j+2}{2}, (i+j = 2,3,\cdots). \quad (9)$$

The Hu moment of contour as:

$$hu[0] = \eta_{2,0} + \eta_{0,2}, \quad (10)$$

$$hu[1] = (\eta_{2,0} - \eta_{0,2})^2 + \eta_{1,1}^4, \quad (11)$$

$$hu[2] = (\eta_{3,0} - 3\eta_{1,2})^2 + (3\eta_{2,1} - \eta_{0,3})^2, \quad (12)$$

$$hu[3] = (\eta_{3,0} + \eta_{1,2})^2 + (\eta_{2,1} + \eta_{0,3})^2, \quad (13)$$

$$\begin{aligned} hu[4] = {} & (\eta_{3,0} - 3\eta_{1,2})(\eta_{3,0} + \eta_{1,2}) \\ & \left[(\eta_{3,0} + \eta_{1,2})^2 - 3(\eta_{2,1} + \eta_{0,3})^2\right] \\ & + (3\eta_{2,1} - \eta_{0,3})(\eta_{2,1} + \eta_{0,3}) \\ & \left[3(\eta_{3,0} + \eta_{1,2})^2 - (\eta_{2,1} + \eta_{0,3})^2\right] \end{aligned}, \quad (14)$$

$$\begin{aligned} hu[5] = {} & (\eta_{2,0} - \eta_{0,2})\left[(\eta_{3,0} + \eta_{1,2})^2 - (\eta_{2,1} + \eta_{0,3})^2\right] \\ & + 4\eta_{1,1}(\eta_{3,0} + \eta_{1,2})(\eta_{2,1} + \eta_{0,3}), \end{aligned} \quad (15)$$

$$\begin{aligned} hu[6] = {} & (3\eta_{2,1} - \eta_{0,3})(\eta_{3,0} + \eta_{1,2}) \\ & \left[(\eta_{3,0} + \eta_{1,2})^2 - 3(\eta_{2,1} + \eta_{0,3})^2\right] \\ & - (\eta_{3,0} - 3\eta_{1,2})(\eta_{2,1} + \eta_{0,3}) \\ & \left[3(\eta_{3,0} + \eta_{1,2})^2 - (\eta_{2,1} + \eta_{0,3})^2\right] \end{aligned}. \quad (16)$$

Formula above is used to calculate the Hu moment value of the keyhole contour in each frame, and those values are used as the feature value of the keyhole shape.

C. WELD FEATURE INFORMATION EXTRACTION

Extract the welding seam image with a width of 70 pixels behind the keyhole position, then perform OTSU threshold segmentation [48] and morphological filtering processing on it. The comparison between original image and processed image is shown in Fig. 2.

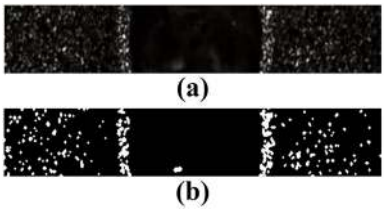

FIGURE 2. (a)Original weld image; (b)Processed weld image.

For the image shown in Fig. 2(b), the following method is used to locate the weld position.

Take a 5 (width) * 70 (height) subset of the image and scan from left to right. When the number of white points in the image is greater than 60%, take the column number of the center column of the subset and record it as C_1. For another edge of weld, take a subset of the same size and scan from right to left. When the number of white points in the image is greater than 60%, take the column number of the center column of the subset and record it as C_2. The weld width can be obtained by the formula as:

$$W = (C_2 - C_1) * std, \quad (17)$$

where C_1, C_2 represents column number of the image corresponding to the center of the left and right weld edges; std represents calibration of camera, the unit is $mm/pixel$; W represents weld width.

The 7 Hu moment values and the feature value of the weld width are taken as the features extracted from the image, and the classification algorithm of machine learning take those values as input to evaluate the quality of the weld.

III. IMAGE FEATURES AND WELD QUALITY EVALUATION

Traditional machine learning classification algorithms (such as SVM [49], etc.) still lack support for multi-classification problems, meanwhile the neural network has higher fitting ability and accuracy, and has better robustness [50].

In this section, 7 HU moment values and weld width were used as inputs to construct BP neural network as shown in Fig. 3.

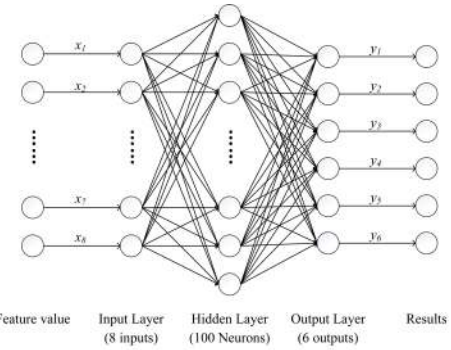

FIGURE 3. Single hidden layer BP neural network structure.

A BP neural network with 100 neurons in a single hidden layer is constructed, and 8 feature values calculated based on the image are used as input to identify defects in the image. The 6 outputs correspond to the Sound well weld state, Lack of fusion state, Burn through state, Dislocation state, Large gap state and Inclusion state in the welding quality respectively.

This article has been accepted for publication in a future issue of this journal, but has not been fully edited. Content may change prior to final publication. Citation information: DOI 10.1109/ACCESS.2021.3108462, IEEE Access

The BP neural network constructed in this section only processes 8 feature values instead of directly processing the image, which greatly reduces the amount of calculation and reduces unnecessary information interference, which helps to achieve high-speed image processing capabilities.

IV. EXPERIMENTAL SYSTEM AND DATASET

A. EXPERIMENTAL SYSTEM

The experimental system includes: a laser welding system with shielding gas and an imaging acquisition system with auxiliary light. Fig. 4(a) shows the general schematic diagram, and Fig. 4(b) shows our experimental equipment.

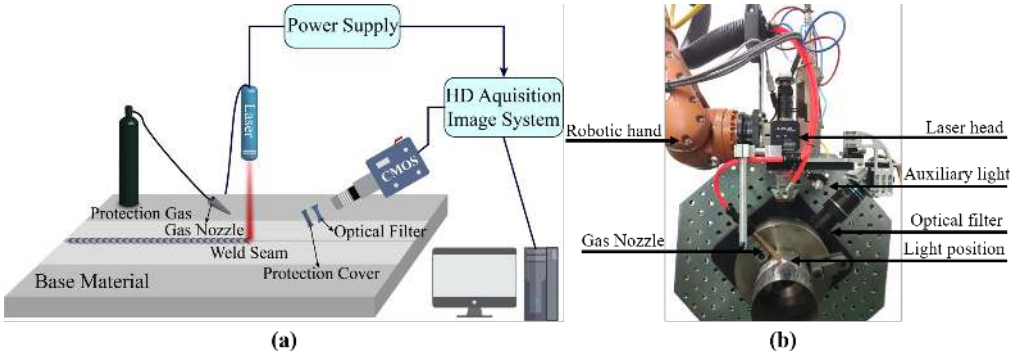

FIGURE 4. **(a) Schematic diagram of experimental equipment; (b) Actual hardware.**

The laser system used a fiber laser with a wavelength of 1064±10nm. The laser beam was focused on the working surface through a defocus lens with a spot diameter of 0.4mm. Welding parameters are shown in Table I. This set of parameters was adopted in all experimental data to ensure the consistency of feature extraction and training standards, as well as the quality of welding. During the welding process, the base material was clamped to a rotating device weighing several hundred kilograms. Due to the huge mass of the transmission device, it took some time to accelerate or slow down the welding speed to reach uniform speed.

TABLE I
WELDING PARAMETERS

Type	Value
Laser type	IPG YLS-6000K 1064nm
Laser head type	IPG P30-010595 FLW D50
Welding speed (mm/s)	2000
Argon flow rate (L/min)	20
Gas nozzle to welding plane distance	255(mm)
Gas nozzle to welding plane angle	90(degree)
Laser power (W)	1850
Spot diameter (mm)	0.4

In this paper, high-power laser welding experiments were conducted on 2 mm thick, 1420°C melting point 304 stainless steel, which is widely used in industry and has significant defect features.

The HD image acquisition system used Optronis CP70-12-M-167 camera with Active Silicon AS-FBD-4XCXP6-2PE8 image acquisition card. The system had 4000FPS, 480pix*480pix RGB image acquisition capabilities. The monitoring parameters are shown in Table II.

TABLE II
MONITORING PARAMETERS

Type	Value
Shutter speed (μs)	50
Frame rate (FPS)	1500
Camera to welding plane distance (mm)	160
Camera to welding plane angle (degree)	40

In the monitoring of the welding process, the high-speed camera directly obtained the RGB image of welding. For imaging, metal vapor and plasma splash were high intensity interference light sources, so it was difficult to achieve ideal results by directly observing holes.

Our attempts have shown that the use of lasers with a central wavelength of about 1064 nm and austenitic stainless steel, a narrow-band filter of about 808 nm and auxiliary illumination laser of the same wavelength could well suppress interference from plasma and metal splash, and the interference of metal vapor could be removed more than 95% by using an anti-interference algorithm based on dark channel prior. The whole experimental device was placed on the robotic hand, which allows us to conveniently load and accurately locate the welding position during the debugging process.

A Windows computer equipped with AMD Ryzen 5900X CPU, 64G RAM, and GTX1650 GPU was used in the image processing system. In this paper, the GenICam TransportLayer API, OpenCV API and the C++ programing language were respectively used to collect images, extract the image features and run the BP neural network algorithm.

B. DATASET

In this paper, three kinds of welding defects which are closely related to the shape of keyhole and two kinds of welding defects which are very sensitive to the weld width were analyzed, namely, the Dislocation, the Large gap, the inclusion, the lack of fusion and the burn through. The first three could be collectively referred to as defects generated by the assembly, the last two for penetration defects. The actual weld image is shown in Fig. 5.

This article has been accepted for publication in a future issue of this journal, but has not been fully edited. Content may change prior to final publication. Citation information: DOI 10.1109/ACCESS.2021.3108462, IEEE Access

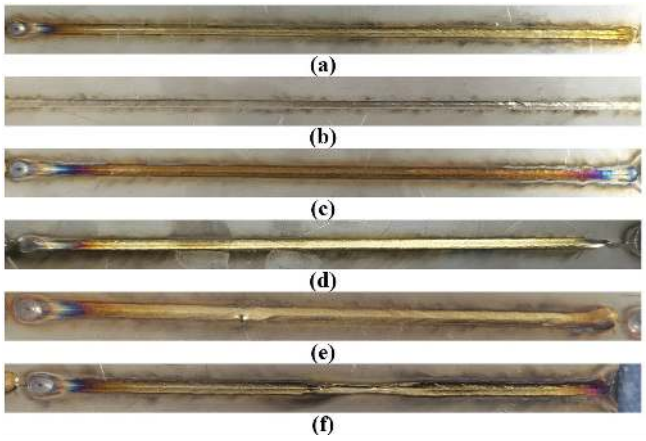

FIGURE 5. **(a)Sound well weld; (b)Lack of fusion; (c)Burn through; (d)Dislocation; (e)Inclusion; (f)Large gap.**

Due to the large mass of the transmission drive, a stable welding speed couldn't be achieved immediately when welding was first started, and this part of the image data needed to be discarded. Same thing at the end. In order to obtain enough data for training and testing, experiment used the parameters in Table I (1450 W for the lack of fusion state; 2150 W for the burn through state, and the rest of states refer to Table I). A total of 7129 pieces 512pix*512pix image of welding image data of 304 stainless steel were collected under different welding conditions. It was divided into six-classifications by experienced welding engineers, namely sound well weld state (1000 samples), lack of fusion state (1000 samples), burn through state (976 samples), Dislocation state (326 samples), Large gap state (826 samples) and inclusion state (3001 samples). Divide the data corresponding to the six welding states into four different datasets as shown in Table III, IV, V and VI. Dataset A corresponds to the binary classification test of whether there were defects. Datasets B and C correspond to the sensitivity between feature information and each defect of assembly defects and penetration defects, respectively. In Dataset D, all defects were identified together to test the model's ability to identify all defects. All the data were subsets of the same complete dataset.

TABLE III
DATASET A: BINARY CLASSIFICATION TEST

Label	Samples	Cross-Validation
Sound well weld	1000	
Defects	6129	
Total	7129	5-fold

TABLE IV
DATASET B: ASSEMBLY DEFECTS CLASSIFICATION TEST

Label	Samples	Cross-Validation
Sound well weld	1000	
Dislocation	326	
Large gap	826	
Inclusion	3001	
Total	5153	5-fold

TABLE V
DATASET C: PENETRATION DEFECTS CLASSIFICATION TEST

Label	Samples	Cross-Validation
Sound well weld	1000	
Lack of fusion	1000	
Burn through	976	
Total	2976	5-fold

TABLE VI
DATASET D: SIX-CLASSIFICATION TEST FOR ALL DEFECTS

Label	Samples	Cross-Validation
Sound well weld	1000	
Lack of fusion	1000	
Burn through	976	
Dislocation	326	
Large gap	826	
Inclusion	3001	
Total	7129	5-fold

C. DATA PROCESSING

The flowchart of entire process is shown in Fig.6. The flowchart of entire process is shown in Fig.6. In the data processing part, the images in the dataset were first processed by the anti-interference algorithm, then the images were respectively processed by the keyhole feature information extraction algorithm and the weld feature information extraction algorithm, and finally the extracted feature values (7 Hu moment values and 1 weld width value) were used for the training of BP neural network.

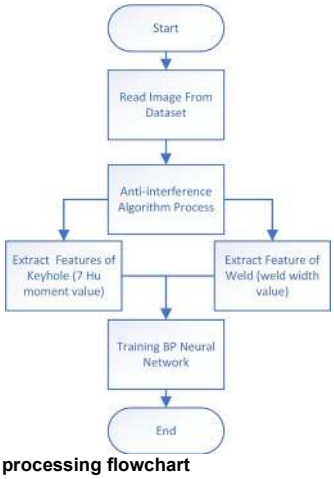

FIGURE 6. **Data processing flowchart**

V. EXPERIMENTAL RESULTS

In this paper, Dataset A is used to verify the influence of anti-interference algorithm on the accuracy of feature extraction. Datasets B and C is used to verify the sensitivity of the classification method to assembly defects and penetration defects, respectively. Dataset D is used to verify the identification effect of all six classification defects.

A. INFLUENCE OF ANTI-INTERFERENCE ALGORITHM ON DEFECT IDENTIFICATION

Metal vapor and plasma splash have obvious interference to the feature extraction of welding images. After processing with anti-interference algorithm, the interference of metal

This article has been accepted for publication in a future issue of this journal, but has not been fully edited. Content may change prior to final publication. Citation information: DOI 10.1109/ACCESS.2021.3108462, IEEE Access

vapor and plasma splash in the image is significantly reduced, and the edges of keyhole and weld remains high gradient, which can be effectively identified by the feature extraction algorithm. Comparison of anti-interference algorithm before and after processing is shown in Fig. 7.

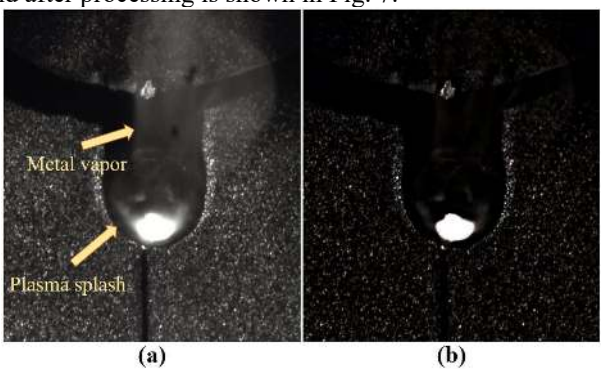

FIGURE 7. **(a)Image before processing; (b)Image after processing ($\omega = 1, \Omega(x) = 5 * 5$, for keyhole's feature extraction).**

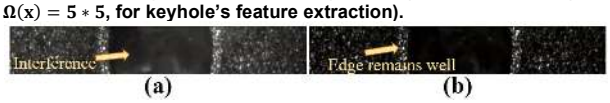

FIGURE 8. **(a) Image before processing; (b)Image after processing ($\omega = 0.9, \Omega(x) = 5 * 5$, for weld's feature extraction).**

The core of the anti-interference algorithm used in this paper is the haze removal algorithm. And traditional indicators for evaluating haze removal algorithms usually include PSNR (Peak Signal-to-Noise Ratio) and SSIM (Structural Similarity) [51]. Since the essence of welding image processing is to remove interference information, and after processing, a large amount of texture information that is not related to feature extraction is removed from the image. The evaluation indicators of traditional haze removal algorithms are difficult to evaluate the effect of anti-interference algorithms proposed in this paper. Therefore, the classification results of the neural network and traditional machine learning algorithm are used in this paper to evaluate the effect of anti-interference processing. Traditional machine learning algorithm (SVM [49], KNN (K-Nearest-Neighbors) [52], Naive Bayes Model [53]) and single hidden layer BP neural network are used to conduct binary classification test on Dataset A, and the results are shown in Table VII. All models use the same inputs and outputs (8 feature value which is 7 Hu moment and 1 weld width as inputs and 2 class which is with and without defects as outputs).

All comparison method were trained in MATLAB R2020a.

In the SVM model, we choose the parameters as kernel: Gaussian kernel which is also called Radial Basis Function (RBF) kernel, Kernel scale: 2.6, Box constraint level: 1, Multiclass method: one vs one, Standardize data: true. In the KNN model, we choose the parameters as Number of neighbors: 100, Distance metric: Euclidean, Distance weight: Equal, Standardize data: true. In the Naïve Bayes Model, we choose the parameters as Distribution name for numeric predictors: Kernel, Distribution name for categorical predictors: MVMN, Kernel type: Gaussian, Support: Unbounded.

TABLE VII
ACCURACY COMPARISON OF ANTI-INTERFERENCE ALGORITHM BEFORE AND AFTER PROCESSING UNDER DIFFERENT CLASSIFICATION ALGORITHMS

Algorithm	Original image (%)	After anti-interference image (%)
SVM	86.7	93.6
KNN	86.3	91.1
Naive Bayes Model	74.0	77.7
BP neural network	92.1	97.2
MAX	92.1	97.2

As shown in Table VII, the accuracy of all method was increased and the maximum accuracy improvement was 6.9% in SVM model. Obviously, after the anti-interference algorithm, the weld state features could be extracted more accurately and more representative of the image.

B. IDENTIFICATION RESULTS OF WELD DEFECTS

To ensure that the classification algorithm has sufficient generalization capability, this paper uses a 5-fold cross-validation [54] approach for training. Fig. 9 - 12 shows the BP neural network confusion matrix of Dataset A, Dataset B, Dataset C, Dataset D, respectively. The numbers in the green squares represent the number of samples for which the predicted value of the neural network is the same as the target value, i.e., the number of correctly classified samples; the numbers in the red squares represent the number of samples for which the predicted value of the neural network is different from the target value, i.e., the number of incorrectly classified samples.

Predict\Target	Defects	Sound well weld	%
Defects	5972	44	99.27
Sound well weld	157	956	85.89
%	97.44	95.60	97.18

FIGURE 9. **Confusion matrix of binary classification test.**

Predict\Target	Sound well weld	Dislocation	Large gap	Inclusion	%
Sound well weld	946	7	5	44	94.41
Dislocation	19	310	3	132	66.81
Large gap	5	6	813	36	94.53
Inclusion	30	3	5	2789	98.66
%	94.60	95.09	98.43	92.94	94.28

FIGURE 10. **Confusion matrix of assembly defects classification test.**

This article has been accepted for publication in a future issue of this journal, but has not been fully edited. Content may change prior to final publication. Citation information: DOI 10.1109/ACCESS.2021.3108462, IEEE Access

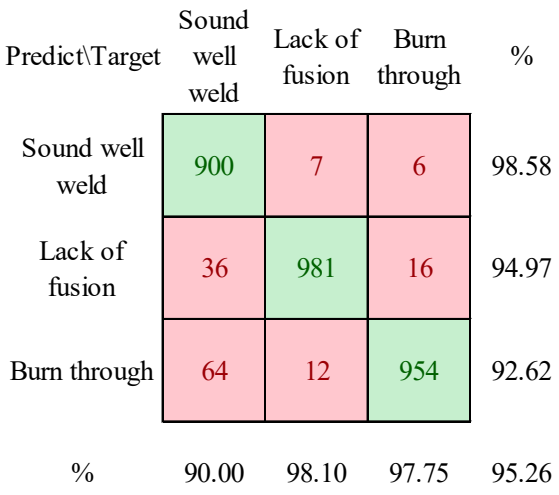

FIGURE 11. **Confusion matrix of penetration defects classification test.**

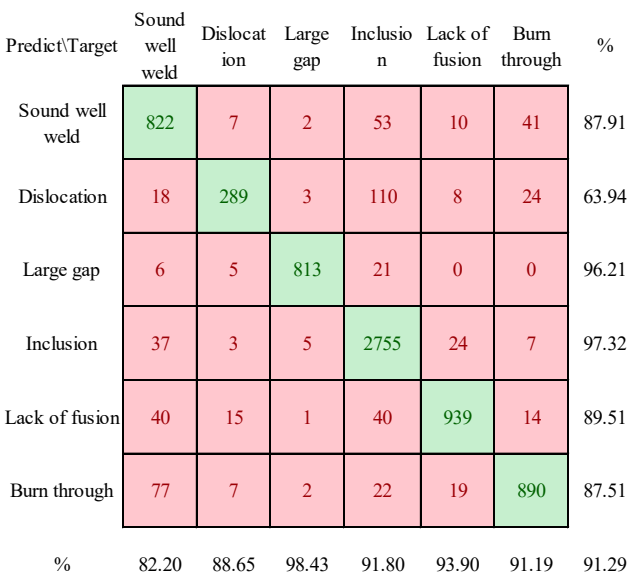

FIGURE 12. **Confusion matrix of six-classification test.**

It can be seen from Fig. 9 that for the binary classification test, the trained BP neural network model can obtain a classification accuracy of 98.37%. The misjudgment is due to the fact that the features of some defect images are similar to those of sound well weld images, mainly lack of fusion images, which can also be seen in Fig. 11. The main feature difference between the lack of fusion images and the sound well weld images is only in weld width, while the feature weight of single feature information is limited in the process of neural network calculation, which is easy to cause the misjudgment of defects. It can be seen from Fig. 10 and 12 that the classification accuracy of defects with Large gap is the highest in both the assembly defect classification test and the last six-classification test. This is because the Large gap defects have significant changes in the shape of the keyhole and the width of weld, and are significantly different from other defects. It can be seen from Fig. 10 and 12 that various types of defects are easily classified as Dislocation defect.

This is because in the image of Dislocation defect, the weld width does not change significantly, and the features of keyhole fluctuate significantly. Some image of Dislocation defect has some similarities with all kinds of defects in the shape of the keyhole and the width of the weld. In the final six-classification test, the classification accuracy of various types of welding images ranged from 82.20% to 98.43%, and the overall classification accuracy was 91.29%. And the time of entire procedure is about 0.3ms which include system I/O spending, anti-interference algorithm spending, feature extraction algorithm spending and BP neural network spending in ours experiment computer.

As for the multi-classification results of the comparison method and our method, they are shown in the Table VIII.

TABLE VIII
ACCURACY COMPARISON OF COMPARISON METHOD AND OUR METHOD

Algorithm	Total accuracy (%)
SVM	60.9
KNN	57.4
Naive Bayes Model	51.5
BP neural network	91.3
MAX	91.3

As shown above, our method has much higher accuracy. That is because for SVM model, it was designed with poor support for multiple classification problems, because it was designed for binary classification problems. For KNN model, its support for multi-classification problems is well, but it is difficult to classify complex data because KNN processes data in original dimension, not higher dimension. For naive bayes model, due to its assumption of sample independence, the classification effect is not good when the sample attributes are correlated with each other. In our data, the samples are related to each other. This gives it the lowest accuracy in binary classification.

In conclusion, the anti-interference algorithm can significantly improve the classification accuracy of the various algorithm. In the BP neural network algorithm, the classification accuracy can be improved by 5.1%. Since the dataset is continuously sampled from the welding video, it can reflect the real welding conditions well and has good generalization ability. Due to the combined effect of the keyhole features and the weld width feature, the BP neural network algorithm has the highest classification accuracy for Large gap defect, which can reach 98.43% in the most demanding six-classification test. The processing time of the entire algorithm is about 0.3ms and it can meet the real-time requirements of high-speed laser welding. And the proposed algorithm only requires a visual-light camera and a computer.

C. TIME COMPLEXITY ANALYSIS OF ALGORITHM

The image size in our dataset is 512pix*512pix. When image size increases, time cost mainly increases in the feature extraction part. The time complexity of feature extraction part is $O(n^2)$ and the other part of our algorithm is $O(n)$. In general, our algorithm's time complexity is $O(n^2)$.

This article has been accepted for publication in a future issue of this journal, but has not been fully edited. Content may change prior to final publication. Citation information: DOI 10.1109/ACCESS.2021.3108462, IEEE Access

VI. CONCLUSION

In the high-power laser welding process, metal vapor and plasma splash can greatly interfere with the feature information of weld quality. Therefore, it is difficult to extract feature information for weld quality evaluation, and establish a direct correspondence between weld image features and weld quality. To solve the above problems, this paper uses an anti-interference algorithm based on dark channel prior to process the image, and uses the trained BP neural network model to identify the defect by using the keyhole features and weld width feature. Experiments have proved that the algorithm can effectively remove the interference of metal vapor and plasma splash on the welding quality feature information, and can accurately identify defects in the feature information of the welding image. It can achieve an overall classification accuracy of 97.18% in the binary classification test, and 91.29% in the six-classification test. The processing time of the entire algorithm is about 0.3ms and it can meet the real-time requirements of high-speed laser welding. And the proposed algorithm only requires a visual-light camera and a computer. However, the classification accuracy of the model will be affected by imaging. And for different kinds of materials, the configuration of the imaging system needs to be redesigned and the model needs to be retrained. In summary, our approach needs to be redesigned or retrained for different materials or different imaging system.

REFERENCES

[1] S. Katayama and Y. Kawahito, "Elucidation of phenomena in high-power fiber laser welding and development of prevention procedures of welding defects," in *Fiber lasers VI: technology, systems, and applications*, 2009, vol. 7195: International Society for Optics and Photonics, p. 71951R.

[2] D. Zhang, M. Wang, C. Shu, Y. Zhang, D. Wu, and Y. Ye, "Dynamic keyhole behavior and keyhole instability in high power fiber laser welding of stainless steel," *Optics & Laser Technology,* vol. 114, pp. 1-9, 2019.

[3] D. You, X. Gao, and S. Katayama, "Review of laser welding monitoring," *Science and technology of welding and joining,* vol. 19, no. 3, pp. 181-201, 2014.

[4] D. You, X. Gao, and S. Katayama, "Visual-based spatter detection during high-power disk laser welding," *Optics and Lasers in Engineering,* vol. 54, pp. 1-7, 2014.

[5] T. Mai and A. Spowage, "Characterisation of dissimilar joints in laser welding of steel–kovar, copper–steel and copper–aluminium," *Materials Science and Engineering: A,* vol. 374, no. 1-2, pp. 224-233, 2004.

[6] Y. Wang, Y. Sun, P. Lv, and H. Wang, "Detection of line weld defects based on multiple thresholds and support vector machine," *Ndt & E International,* vol. 41, no. 7, pp. 517-524, 2008.

[7] C. L. A. Leung, S. Marussi, R. C. Atwood, M. Towrie, P. J. Withers, and P. D. Lee, "In situ X-ray imaging of defect and molten pool dynamics in laser additive manufacturing," *Nature communications,* vol. 9, no. 1, pp. 1-9, 2018.

[8] D. Du, R. Hou, J. Shao, B. Chang, and L. Wang, "Registration of real-time X-ray image sequences for weld inspection," *Nondestructive Testing and Evaluation,* vol. 25, no. 2, pp. 153-159, 2010.

[9] P. L. Zhang, Z. Q. Zhao, and Y. P. Wang, "X-Ray Testing of Weld Defect of Automatic Recognit Ion and Alarm Technology Research," in *Applied Mechanics and Materials*, 2014, vol. 472: Trans Tech Publ, pp. 495-502.

[10] Y. Javadi *et al.*, "Continuous monitoring of an intentionally-manufactured crack using an automated welding and in-process inspection system," *Materials & Design,* p. 108655, 2020.

[11] S. Nath, K. Balasubramaniam, C. Krishnamurthy, and B. Narayana, "Detection and sizing of defects in complex geometry weld by manual ultrasonic time of flight diffraction inspection," *Journal of pressure vessel technology,* vol. 131, no. 5, 2009.

[12] X. Xiao, B. Gao, G. yun Tian, and K. qing Wang, "Fusion model of inductive thermography and ultrasound for nondestructive testing," *Infrared Physics & Technology,* vol. 101, pp. 162-170, 2019.

[13] Y. Javadi *et al.*, "Investigating the effect of residual stress on hydrogen cracking in multi-pass robotic welding through process compatible non-destructive testing," *Journal of Manufacturing Processes,* 2020.

[14] Y. Javadi *et al.*, "Ultrasonic phased array inspection of a Wire+ Arc Additive Manufactured (WAAM) sample with intentionally embedded defects," *Additive Manufacturing,* vol. 29, p. 100806, 2019.

[15] R. Ranjan *et al.*, "Classification and identification of surface defects in friction stir welding: An image processing approach," *Journal of Manufacturing Processes,* vol. 22, pp. 237-253, 2016.

[16] P. Sassi, P. Tripicchio, and C. A. Avizzano, "A smart monitoring system for automatic welding defect detection," *IEEE Transactions on Industrial Electronics,* vol. 66, no. 12, pp. 9641-9650, 2019.

[17] R. Hartl, A. Bachmann, S. Liebl, A. Zens, and M. Zaeh, "Automated surface inspection of friction stir welds by means of structured light projection," in *IOP Conference Series: Materials Science and Engineering*, 2019, vol. 480, p. 012035.

[18] J. Ye, G. Xia, B. Hu, and Q. Cheng, "Comprehensive detection method of weld based on line structured light and weak magnetic detection," in *Ninth International Symposium on Precision Mechanical Measurements*, 2019, vol. 11343: International Society for Optics and Photonics, p. 113430R.

[19] Y. Huang, G. Li, W. Shao, S. Gong, and X. Zhang, "A novel dual-channel weld seam tracking system for aircraft T-joint welds," *The International Journal of Advanced Manufacturing Technology,* vol. 91, no. 1-4, pp. 751-761, 2017.

[20] Y. Li, Q. L. Wang, Y. F. Li, D. Xu, and M. Tan, "On-line visual measurement and inspection of weld bead using structured light," in *2008 IEEE Instrumentation and Measurement Technology Conference*, 2008: IEEE, pp. 2038-2043.

[21] Y. Han, J. Fan, and X. Yang, "A structured light vision sensor for on-line weld bead measurement and weld quality inspection," *The International Journal of Advanced Manufacturing Technology,* vol. 106, no. 5, pp. 2065-2078, 2020.

[22] S. S. Indimath, R. Shunmugasundaram, S. Balamurugan, M. Dutta, S. K. Gudimetla, and K. Kant, "Online ultrasonic technique for assessment of mash seam welds of thin steel sheets in a continuous galvanizing line," (in English), *Int. J. Adv. Manuf. Technol.,* Article vol. 91, no. 9-12, pp. 3481-3491, Aug 2017, 10.1007/s00170-017-9995-8.

[23] F. Dorsch, H. Braun, S. Kessler, D. Pfitzner, and V. Rominger, "Online characterization of laser beam welds by NIR-camera observation," in *High-Power Laser Materials Processing: Lasers, Beam Delivery, Diagnostics, and Applications Ii*, vol. 8603, F. Dorsch Ed., (Proceedings of SPIE, 2013.

[24] R. Miao *et al.*, "Online inspection of narrow overlap weld quality using two-stage convolution neural network image recognition," *Machine Vision and Applications,* vol. 32, no. 1, Feb 2021, Art no. 27, 10.1007/s00138-020-01158-2.

[25] X. Na, Y. Zhang, Y. Liu, and B. Walcott, "Nonlinear identification of laser welding process," *IEEE transactions on control systems technology,* vol. 18, no. 4, pp. 927-934, 2009.

[26] X. Gao, L. Wang, Z. Chen, Y. Zhang, and D. You, "Process stability analysis and weld formation evaluation during disk laser–mag hybrid welding," *Optics and Lasers in Engineering,* vol. 124, p. 105835, 2020.

[27] D. Farson, "Progress in real time laser process monitoring: theory and practice," *Science and technology of welding and joining,* vol. 5, no. 3, pp. 194-201, 2000.

[28] J. Stavridis, A. Papacharalampopoulos, and P. Stavropoulos, "Quality assessment in laser welding: a critical review," *The International Journal of Advanced Manufacturing Technology,* vol. 94, no. 5, pp. 1825-1847, 2018.

[29] G. Li, Y. Cai, and Y. Wu, "Stability information in plasma image of high-power CO2 laser welding," *Optics and Lasers in Engineering,* vol. 47, no. 9, pp. 990-994, 2009.

[30] S. Katayama, S. Kawaguchi, M. Mizutani, Y. Kawahito, and T. Tarui, "Welding phenomena and in-process monitoring in high-power YAG laser welding of aluminium alloy," *Welding International,* vol. 23, no. 10, pp. 753-762, 2009.

[31] Q. Wen and X. D. Gao, "Classification of plume image and analysis of welding stability during high power disc laser welding," in *Applied Mechanics and Materials*, 2012, vol. 201: Trans Tech Publ, pp. 1139-1142.

[32] Y. Zhang, Z. Zhao, Y. Zhang, L. Bai, K. Wang, and J. Han, "Online weld pool contour extraction and seam width prediction based on mixing spectral vision," *Optical Review,* vol. 26, no. 1, pp. 65-76, 2019.

[33] B. Chen, Y. Yao, Y. Huang, W. Wang, C. Tan, and J. Feng, "Quality detection of laser additive manufacturing process based on coaxial vision monitoring," *Sensor Review,* 2019.

[34] L. Armi and S. Fekri-Ershad, "Texture image analysis and texture classification methods-A review," *arXiv preprint arXiv:1904.06554,* 2019.

[35] S. Fekri-Ershad and F. Tajeripour, "A robust approach for surface defect detection based on one dimensional local binary patterns," *Indian Journal of Science and Technology,* vol. 5, no. 8, pp. 3197-3203, 2012.

[36] F. Timm and E. Barth, "Non-parametric texture defect detection using Weibull features," in *Image Processing: Machine Vision Applications IV*, 2011, vol. 7877: International Society for Optics and Photonics, p. 78770J.

[37] S. Susan and M. Sharma, "Automatic texture defect detection using Gaussian mixture entropy modeling," *Neurocomputing,* vol. 239, pp. 232-237, 2017.

[38] S. A. Shevchik *et al.*, "Laser welding quality monitoring via graph support vector machine with data adaptive kernel," *IEEE Access,* vol. 7, pp. 93108-93122, 2019.

[39] Y. Chen, B. Chen, Y. Yao, C. Tan, and J. Feng, "A spectroscopic method based on support vector machine and artificial neural network for fiber laser welding defects detection and classification," *NDT & E International,* vol. 108, p. 102176, 2019.

[40] Y. Zhang, D. You, X. Gao, N. Zhang, and P. P. Gao, "Welding defects detection based on deep learning with multiple optical sensors during disk laser welding of thick plates," *Journal of Manufacturing Systems,* vol. 51, pp. 87-94, 2019.

[41] S. Shevchik *et al.*, "Supervised deep learning for real-time quality monitoring of laser welding with X-ray radiographic guidance," *Scientific reports,* vol. 10, no. 1, pp. 1-12, 2020.

[42] D. You, X. Gao, and S. Katayama, "WPD-PCA-based laser welding process monitoring and defects diagnosis by using FNN and SVM," *IEEE Transactions on Industrial Electronics,* vol. 62, no. 1, pp. 628-636, 2014.

[43] J. Shao, Y. Yan, and Ieee, "Automated inspection of micro laser spot weld quality using optical sensing and neural network techniques," in *2006 Ieee Instrumentation and Measurement Technology Conference Proceedings, Vols 1-5*, (IEEE Instrumentation and Measurement Technology Conference, 2006, pp. 606-+.

[44] K. He, J. Sun, and X. Tang, "Single image haze removal using dark channel prior," *IEEE transactions on pattern analysis and machine intelligence,* vol. 33, no. 12, pp. 2341-2353, 2010.

[45] F. Huang, G. Li, C. Zou, C. Liu, and H. Wang, "Adaptive image dehazing based on dark channel prior," *Journal of Optoelectronics·Laser,* vol. 30, no. 12, pp. 1323-1330, 2019 2019, Art no. 1005-0086(2019)30:12<1323:Aysxyz>2.0.Tx;2-#.

[46] K. He, J. Sun, and X. Tang, "Guided image filtering," *IEEE transactions on pattern analysis and machine intelligence,* vol. 35, no. 6, pp. 1397-1409, 2012.

[47] M.-K. Hu, "Visual pattern recognition by moment invariants," *IRE transactions on information theory,* vol. 8, no. 2, pp. 179-187, 1962.

[48] N. Otsu, "A threshold selection method from gray-level histograms," *IEEE transactions on systems, man, and cybernetics,* vol. 9, no. 1, pp. 62-66, 1979.

[49] C.-C. Chang and C.-J. Lin, "LIBSVM: A library for support vector machines," *ACM transactions on intelligent systems and technology (TIST),* vol. 2, no. 3, pp. 1-27, 2011.

[50] P. Werbos, "Beyond regression:" new tools for prediction and analysis in the behavioral sciences," *Ph. D. dissertation, Harvard University,* 1974.

[51] L. M. Devi, K. Wahengbam, and A. D. Singh, "Dehazing buried tissues in retinal fundus images using a multiple radiance pre-processing with deep learning based multiple feature-fusion," *Optics & Laser Technology,* vol. 138, p. 106908, 2021.

[52] N. S. Altman, "An introduction to kernel and nearest-neighbor nonparametric regression," *The American Statistician,* vol. 46, no. 3, pp. 175-185, 1992.

[53] G. I. Webb, J. R. Boughton, and Z. Wang, "Not so naive Bayes: aggregating one-dependence estimators," *Machine learning,* vol. 58, no. 1, pp. 5-24, 2005.

[54] R. Kohavi, "A study of cross-validation and bootstrap for accuracy estimation and model selection," in *Ijcai*, 1995, vol. 14, no. 2: Montreal, Canada, pp. 1137-1145.

YINRUI GAO received the B.S. degree in mechanical engineering from Nanchang University, Nanchang, China, in 2019. He is currently pursuing the M.S. degree in optical engineering with Donghua University, Shanghai, China.

PING ZHONG received the bachelor's degree in computer science from Jilin University, Jilin, China, in June 1996, and the master's and Ph.D. degrees in optical engineering from the Chinese Academy of Sciences, Jilin, in June 2004. He is currently a Professor with Donghua University, Shanghai, China. His research interests include optical metrology, image processing, and optical sensors.

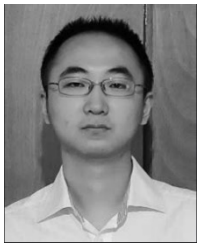

XIN TANG received the B.S. degree in electronic and information engineering from the Shanghai University of Engineering Science. He is currently pursuing the Ph.D. degree in control science and engineering with Donghua University, Shanghai, China. His research interests include optical sensors, image processing, and optical metrology.

This article has been accepted for publication in a future issue of this journal, but has not been fully edited. Content may change prior to final publication. Citation information: DOI 10.1109/ACCESS.2021.3108462, IEEE Access

HAOWEI HU was born in 1996. He received the B.E. degree in optoelectronic information science and engineering from Nanchang Hangkong University, Jiangxi, China, in 2019. He is currently pursuing the M.S. degree in optical engineering with Donghua University, Shanghai, China. His research interests include photoelectric detection and image processing.

PENG XU was born in Anqing, Anhui Province, China, in 1999.
From 2018 to 2020, he was doing research in physical direction with a Professor in the laboratory, including the thermal lens effect of the medium in the light field and its imaging law. He is currently with the Department of Applied Physics, Donghua University.